Journal of the Iranian Chemical Society (2020) 17:2943–2956
https://doi.org/10.1007/s13738-020-01970-7

ORIGINAL PAPER

Doping of Fe on room-temperature-synthesized CoNi layered double hydroxide as an excellent bifunctional catalyst in alkaline media

Anand Parkash[1,2]

Received: 14 April 2020 / Accepted: 1 June 2020 / Published online: 10 June 2020

Abstract

Currently, the high demand for energy results in a large amount of pollution, which is of great concern. To overcome this problem, a highly active and low-cost bifunctional electrocatalyst for the oxygen reduction reaction (ORR) and oxygen evolution reaction (OER) is crucial to satisfy industrial criteria. Layered double hydroxides (LDH) attracted significant interest in several fields, including catalysis, storage of energy, delivery of drug*e*s, etc. A simple coprecipitation method for the preparation of highly active electrochemical Fe_x/CoNi LDH catalysts at room temperature was described here. In alkaline media, from series of prepared catalysts, the $Fe_{8\%}$/Co–Ni LDH shows superior electrocatalytic activity with an overpotential of 232 mV at 10 mA/cm^2, and E_o 91 V and $E_{1/2}$ 0.83 V versus RHE comparable to both noble metal-based and noble-metal-free OER/ORR catalysts recorded. Proper electronic structure and charging resistance that can facilitate the reduction of electron movement in the ORR/OER, are considered as two main factors in reducing the over-potential catalytic reaction.

Graphic abstract

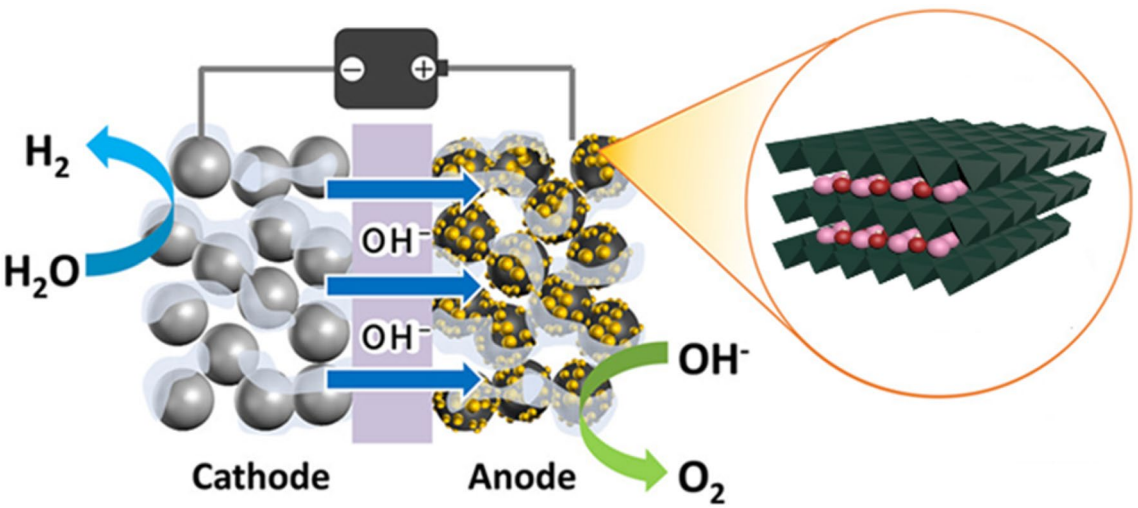

Keywords Fuel cell · Non-noble metal · Layered double hydroxide · OER · ORR

Introduction

The increasing demand for energy and environmental solutions has prompted extensive studies into energy storage systems and methods of conversion, such as metal-air batteries, water decomposition, carbon dioxide capture, fuel cells

Electronic supplementary material The online version of this article (https://doi.org/10.1007/s13738-020-01970-7) contains supplementary material, which is available to authorized users.

✉ Anand Parkash
anand@snnu.edu.cn

Extended author information available on the last page of the article

[1–5]. Electrochemical reactions, such as oxygen evolution reaction (OER), oxygen reduction reaction (ORR), hydrogen reduction reaction (HER), and CO_2 reduction, are the basic steps of these approaches [6–10]. Platinum group metals (PGMs) are active electrocatalysts, but their scarcity and high cost restrict their use in the energy conversion industry [11–13]. Therefore, there is an urgent need to research high-performance and low-cost nonplatinum group metal electrocatalysts [14–16]. The production of appropriate and economic catalysts with high activity, such as non-noble metals/metal oxides and carbon-based materials, is, therefore, of great importance [17–19].

Both specifications can be met using layered double hydroxides (LDH), instead of the traditional anode and cathode materials used in energy systems [20–22]. LDHs are a class of natural and synthetic compounds, and the general formula is $[M(II)_{1-x}M(III)_x(OH)_2](y^{n-})_{x/n}\text{-}yH_2O$, in which M(II) and M(III), respectively, represent divalent and trivalent metals, and Y^{n-} is anion interlayer [23–25]. Divalent metals in today's LDH materials may be Mg^{2+}, Ca^{2+}, Zn^{2+}, Co^{2+}, Cu^{2+}, etc.; trivalent metals may be Al^{3+}, Cr^{3+}, Co^{3+}, Fe^{3+}, Mn^{3+}, etc., [26–29]. Several anions can be used, including several organic anions, including Cl^-, NO_3^-, and CO_3^{2-}[30–33]. LDH is also known as hydrotalcite-like compounds (because these are like minerals in structure) or anion clays [34–36]. These are structurally composed of [Mg $(OH)_2$] brucite-like compounds, with a net positive charge due to partial substitution of divalent metal $(M_2)^+$ trivalent metal (M_3); change usually results in X values between 0.2 and 0.4 [37–40]. The positive charge is effectively distributed evenly on each substratum under the control of the positive charge center's repulsion power [41–43]. Apart from water molecules, anions are often brought into the vacuum of the interlayer to equate the total positive charge with the negative charge. NiFe LDH has become one of the most promising OER catalysts under alkaline conditions thanks to its unique structure and high intrinsic catalytic activity, but its ORR activity is low [44–48]. Electrocatalyst based on LDHs can be used to efficiently and stably prepare the bifunctional electrocatalyst, which is of great importance for solving these problems. It should be noted that LDH materials have low conductivity and a high propensity to form fast aggregation [49–52]. Therefore, designing high-performance bifunctional electrocatalysts by optimizing strategies such as deposition on the conductive substrate, morphology regulation, composition change, and surface modification is of great importance according to the basic structural characteristics of LDHs.

In this study, Fe-doped Co–Ni LDHs (called Fe_x/CoNi LDHs) were synthesized by doping CTAB-capped Fe nanoparticles (NPs) on the surface of CoNi LDH as an excellent bifunctional electrocatalyst. The electrochemical results show that with $Fe_{8\%}$/CoNi LDH at a low overpotential of 232 mV, the current density of 10 mA cm^{-2} can be achieved. The efficiency of ORR (E_o 0.91 V and $E_{1/2}$ 0.81 V) is substantially improved compared with other catalysts and commercial Pt/C and RuO_2. This work provides an effective technique of optimization by doping metal cations on LDHs for catalyst applications, flame retardants, ion exchangers, novel nanocomposites, etc.

Results and discussion

The Fe_x/CoNi LDHs were prepared by a simple coprecipitation method at room temperature with low cost and earth-abundant chemicals as raw materials. A simple two-step room-temperature reaction was used to synthesize a bimetallic CoNi LDH and various contents of doped CTAB-capped Fe nanoparticles nanostructure (see "Experimental" section). Samples have been named according to the Fe content used. Co and Ni are in ratio constant (Table 1). X-ray diffraction (XRD) analyzed the as-prepared sample to analyses phase (Fig. 1). Fe_x/CoNi LDH diffraction peaks at 11.41°, 22.97°, 33.53°, 34.42°, 38.99°, 45.98°, 59.93°, 61.25°, and 61.25° can be indexed to (003), (006), (001), (012), (015), (018), (113), and (116) crystal faces (JCPDS no. 40-0215). The diffraction peaks of all prepared LDHs are a clear indication that Fe doping induces no phase change and should suggest sampling without detectable impurities such as Fe_2O_3 and CoO, etc.

N_2 adsorption–desorption isotherms identified the surface area and porosity of the as-prepared materials and are shown in Fig. 2 and Table 2. As for all as-prepared samples, a type IV isotherm with a type H_4 hysteresis loop, which defines a mesoporous content, may be observed. Brunauer–Emmett–Teller (BET) has a surface area of 108

Table 1 Elemental composition of prepared layered double hydroxide

Catalysts	Theoretical (wt%)			EDX analysis (wt%)		
	Fe	Co	Ni	Fe	Co	Ni
Co–Ni-LDH	–	10	12	–	8.97	10.97
$Fe_{4\%}$/Co–Ni-LDH	4	10	12	6.72	7.88	9.51
$Fe_{6\%}$/Co–Ni-LDH	6	10	12	7.84	8.26	10.92
$Fe_{8\%}$/Co–Ni-LDH	8	10	12	10.19	12.34	8.02
$Fe_{10\%}$/Co–Ni-LDH	10	10	10	11.98	14.01	8.30

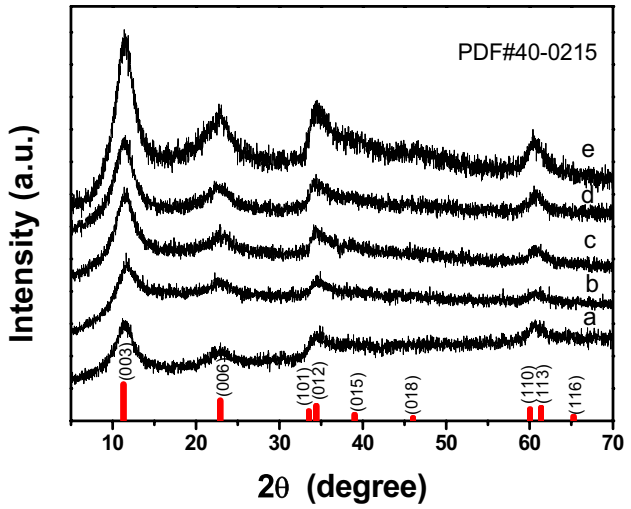

Fig. 1 Powder XRD patterns: **a** Co–Ni-LDH, **b** $Fe_{4\%}$/Co–Ni-LDH, **c** $Fe_{6\%}$/Co–Ni-LDH, **d** $Fe_{8\%}$/Co–Ni-LDH and **e** $Fe_{10\%}$/Co–Ni-LDH

$m^2\ g^{-1}$ of $Fe_{8\%}$/CoNi LDH, relatively higher compared to CoNi LDH (86 $m^2\ g^{-1}$), $Fe_{4\%}$/CoNi LDH (90 $m^2\ g^{-1}$), $Fe_{6\%}$/CoNi LDH (96 $m^2\ g^{-1}$), and $Fe_{10\%}$/CoNi LDH (104 $m^2\ g^{-1}$). These results indicate that the specific area increases with the Fe content increase. We noticed a change in the hysteresis loop because of the different composition of LDH. $Fe_{8\%}$/CoNi LDH is closed at a relative pressure of approximately 0.5 (P/P_0) and has a small platform at a high P/P_0 that is connected to the sample's mesoporous properties [2, 8]. The higher specific surface area and special porous nanostructure will provide a higher catalytic activity for the LDH hybrid, due to the higher density of active centers on the surface of the catalyst and lower resistance to mass transfer [5, 11].

SEM images (Fig. 3) identified the various LDH powder morphologies. The SEM image indicates that the substance is lightweight and is dispersed around its surface with tiny loose little particles. The material morphology is usually uniform. The EDS shows the presence of Co, Fe, Ni, and O, and these elements are added as part of the salts (Fig. 3f). These results indicate that the LDH is pure. The small particles have a distinct form and appear to be made of stacked material. Doping and stirring may have contributed to the size of LDH particles. When applying LDH in ORR/OER, the small crystal sizes seen in this picture are helpful. The Na possibly derived from the synthesis reaction of NaOH, which was used as a protective agent in the synthesis reaction. Figures S2–S7 show the mapping of elements of the synthesized LDH prepared by our new protocol. Such maps clearly show the nickel, cobalt, and iron present in the product. As shown in the map of the elements, these elements are uniformly distributed in the final product, suggesting a uniform composition of the synthesized LDH. Although sharing very similar patterns of PXRD, all samples showed irregular agglomeration, indicating iron may boost LDH morphology. The change of particle size and morphology of LDH may be due to the different crystal growth behavior in the presence of Fe. The elemental composition of LDH samples was determined by EDS (Table 1), which shows that the actual molar ratio of Ni, Fe, and CO in the synthesized LDH is the same as that of the precursor. The EDX results are consistent with the initial content ratio.

TEM and STEM were also used to demonstrate the morphological features of the as-synthesized LDHs to gain more insight into the LDH structures. The corresponding results (Fig. 4, S1) show the uniform distribution of CTAB-capped Fe nanoparticles in LDH, suggesting that Fe has been successfully doped into the LDH. The HRTEM images show that the transparent lattice fringes with a lattice spacing of 0.19 nm are compatible with the crystal plane spacing (012), suggesting the generation of crystal LDH, which also corresponds to the PXRD. It is therefore clear that doping (by impregnation) not only affects the composition of the embedded metal nanoparticles in the LDH matrix but also directly affects their thickness, resulting in a higher degree of the nanostructure.

FTIR was also used for product characterization in LDH materials (Fig. S7). The large and small band observed about 3600–3200 cm^{-1} is correlated with a hydroxyl stretching band (OH) superposition resulting from metal-hydroxyl groups and water molecules with hydrogen-bonded interlay [25]. The hydrogen bonding between water and carbonate can be allocated to the arm in the interlayer, close to 2970 cm^{-1}. Because of absorption, the water bending frequency is 1630 cm^{-1}[15]. The bending mode of water molecules reveals that there is a small amount of interlayer water in the LDH, resulting in a low-resolution band of about 1630 cm^{-1} due to the rich anions in the LDH compensating the positive charge of the layer [33]. The LDH spectrum reveals a wide band centered on 3442 cm^{-1}, which is the superposition of layered hydroxyl and interlayered hydrogen-bonded water molecules due to the OH stretching mode [42]. LDH appeared at 3500 cm^{-1} approx. The electronegativity can alter the electron density of the O–H bond [19]. The interlayer anions and the water molecules are symmetrically bonded with hydrogen for the carbonate LDH formed by M(II) and M(III) [41–44]. At 1370 cm^{-1}, only one band was observed, which means that the carbonate anion symmetry is identical to that of free anion, i.e., Symmetry D_3h[21, 50]. There is a high-strength absorption band at 1385 cm^{-1}, meaning nitrate anion (NO_3^-) is present in the LDH structure. At 1357 cm^{-1}, there is no band, which proves that LDH again lacks CO_3^{2-} anion [17–21]. At 3400 cm^{-1}, the broad absorption band corresponds to the stretching vibration in LDH of unstable hydroxyl or physically adsorbed water molecules [4, 12]. The maximum water bending mode is

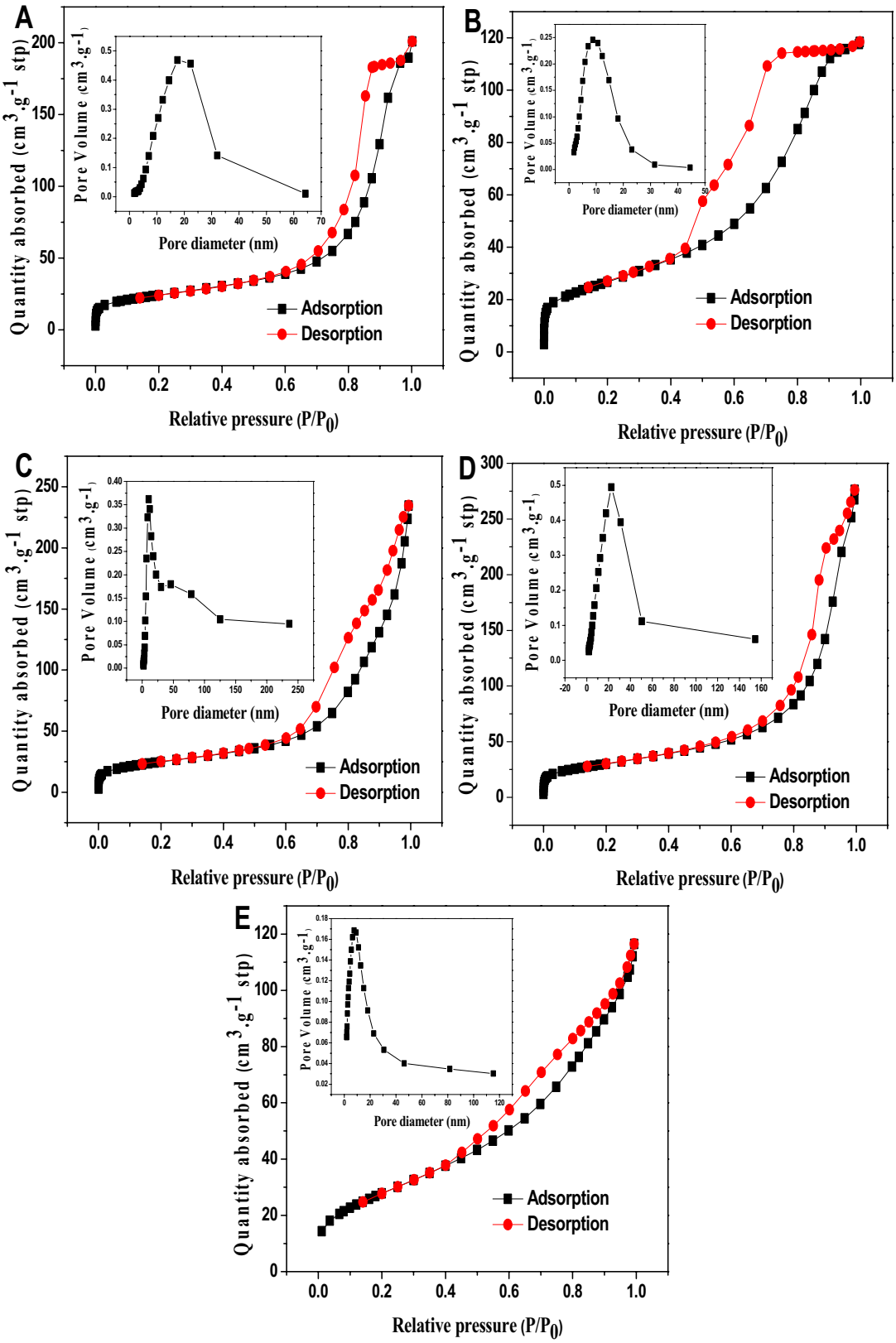

Fig. 2 N_2 adsorption–desorption isotherms: **a** Co–Ni-LDH, **b** $Fe_{4\%}$/Co–Ni-LDH, **c** $Fe_{6\%}$/Co–Ni-LDH, **d** $Fe_{8\%}$/Co–Ni-LDH and **e** $Fe_{10\%}$/Co–Ni-LDH. The inset graphs show the pore size distribution curves of the samples

Table 2 Textural properties of the prepared catalysts

Sample	BET surface (m^2g^{-1})[a]	Pore volume (cm^3g^{-1})[b]	Pore size (nm)[c]
Co–Ni-LDH	86	0.28	12.91
$Fe_{4\%}$/Co–Ni-LDH	90	0.35	14.52
$Fe_{6\%}$/Co–Ni-LDH	96	0.35	14.52
$Fe_{8\%}$/Co–Ni-LDH	108	0.39	14.03
$Fe_{10\%}$/Co–Ni-LDH	104	0.17	6.61

[a]Specific surface area according to BET

[b]Calculated according to BJH analysis (adsorption branch between 1.7 nm and 300 nm diameters)

[c]Adsorption average pore width (4 V/A by BET)

attributable to 1633 cm^{-1}. The absorption peaks of the M–O-H and O-M–O bending and stretching methods are less than 800 cm^{-1} for brucite like materials [31–33]. However, the exchange cannot extract 100% of the parent compounds' nitrate anions. This is evident from the presence of the characteristic peak (NO_3) at 1384 cm^{-1} in the infrared spectrum of the compound [21–23].

X-ray photoelectron spectroscopy (XPS) was used to calculate the chemical states of LDH. The spectra can be deconvoluted into three peaks of oxygen in the area of O1s (Fig. 5), which corresponds to Fe–O (531.65 eV), Ni–O (529.80 eV) and Co–O (531.32 eV). The binding energies of Ni (II) and Ni (III) are closely linked to the peaks at 855.82 eV and 857.58 eV in this respect (Fig. 5d). The binding energy of peaks at 780.96 eV and 783.22 eV is due to the presence of Co (II), and Co (III) species in the LDH indicated by $Co2P_{3/2}$ (Fig. 5c) within the high-resolution range of Co2p. It is worth noting that besides the Fe (III) peak (710.78 eV), another peak appears at the 712.78 eV binding energy, indicating the presence of Fe (IV) in the material.

ORR activities were first evaluated by CV in the 0.1 M KOH solution saturated with N_2 and O_2 at a scan rate of 50 mV s^{-1}. Figure 7a displays the most active $Fe_{8\%}$/CoNi LDH observed in O_2 and N_2 environments. In the O_2-saturated electrolyte solution, which is not present in voltammograms reported under N_2-saturated electrolyte, a well-defined irreversible cathodic peak in the potential range 0.6–0.8 V versus RHE is observed, confirming the ORR activity of $Fe_{8\%}$/CoNi LDH electrocatalyst. Second, the electrocatalytic properties of all ORR LDHs are investigated using a rotating disc electrode (RDE) using linear sweep voltammetry (LSV). Figure 6a displays the LSV curves at 1600 rpm for the various registered LDHs. Most of the calculations are listed in Table 3. These findings indicate that the presence of CTAB-capped Fe nanoparticles improves the electrocatalytic activity of these materials. $Fe_{8\%}$/CoNi-LDH had the highest E_o (0.91 V) and $E_{1/2}$ (0.83 V) levels compared to CoNi-LDH (E_o 0.85 V, $E_{1/2}$ 0.73 V), $Fe_{4\%}$/CoNi-LDH (E_o 0.86 V, $E_{1/2}$ 0.77 V), $Fe_{6\%}$/CoNi-LDH (E_o 0.88 V, $E_{1/2}$ 0.79 V), and $Fe_{10\%}$/CoNi-LDH (E_o 0.90 V, $E_{1/2}$ 0.81 V), respectively (Fig. 6a,c, Table 3). To demonstrate the effect of iron content on LDH synthesis, LSV testing was performed for LDH synthesized under different iron content, and the data obtained are shown in Fig. 6. Results show that LDH with iron content of 8% has high electrocatalytic activity, and its current density is much higher than that of other LDHs. This is because of the increase in the basic surface area and the optimum iron content.

The LSV curve reported before and after 1000 cycles is shown in Fig. 7d. Since the 1000th cycle, the current limit is down slightly. Nonetheless, the strong electrocatalytic activity of $Fe_{8\%}$/CoNi-LDH may be attributable to the synergistic catalysis of their Co, Ni, and Fe species and strong specific surface area attributable to the same CO and Ni content and different Fe content of these materials. On top of that, the electrocatalytic behavior of the ideal ORR catalyst synthesized in alkaline solution is equal to or better than that of several recently published electrocatalysts. Such defects regulate the catalyst's electronic properties and boost the catalyst's performance [27–29]. Coordination of unsaturated metal sites will, therefore, lead to vacancy deficiencies and engineering disorder, which will directly affect the electronic structure of the LDH hybrid, which in effect plays an important role in optimizing the electrochemical properties of the active sites and achieving higher electrochemical efficiency.

Koutecky–Levich (K–L) plots at 0.4 V to 0.7 V (Figs. 6c, 7c, S9), which describe the relation between current density and rotational speed. The excellent linearity of the K–L diagram shows the first-order reaction being the catalytic ORR. The electron transfer number (n) during ORR is also found to be 3.9 based on the slope of the K–L plots, exactly matching the process of reduction of oxygen by 4 electrons. The 4-electron direction is the safest way to reduce oxygen from electrocatalytic [24, 39]. Based on previous studies, the ORR was heavily dependent upon the catalyst size, which is called the particle size effect [19]. At around the same time, the presence of two-electron or four-electron reducing pathways can be affected [25]. Hence the morphology of the electrocatalyst significantly impacted fuel cell performance. The increase in starting potential and the constraining current found in the samples were due primarily to the more active sites [10]. Due to the difference in electronegativity, ORR increases due to changes in load density and spin density arising from the asymmetric charge distribution [8]. The layered prismatic structure of LDHs provides a high BET-specific surface area for ion interaction, which is conducive to charging migration; abundant microporous defects cannot only produce rich active phases around the pores [14], but also significantly enrich the active phases, and provide a wet

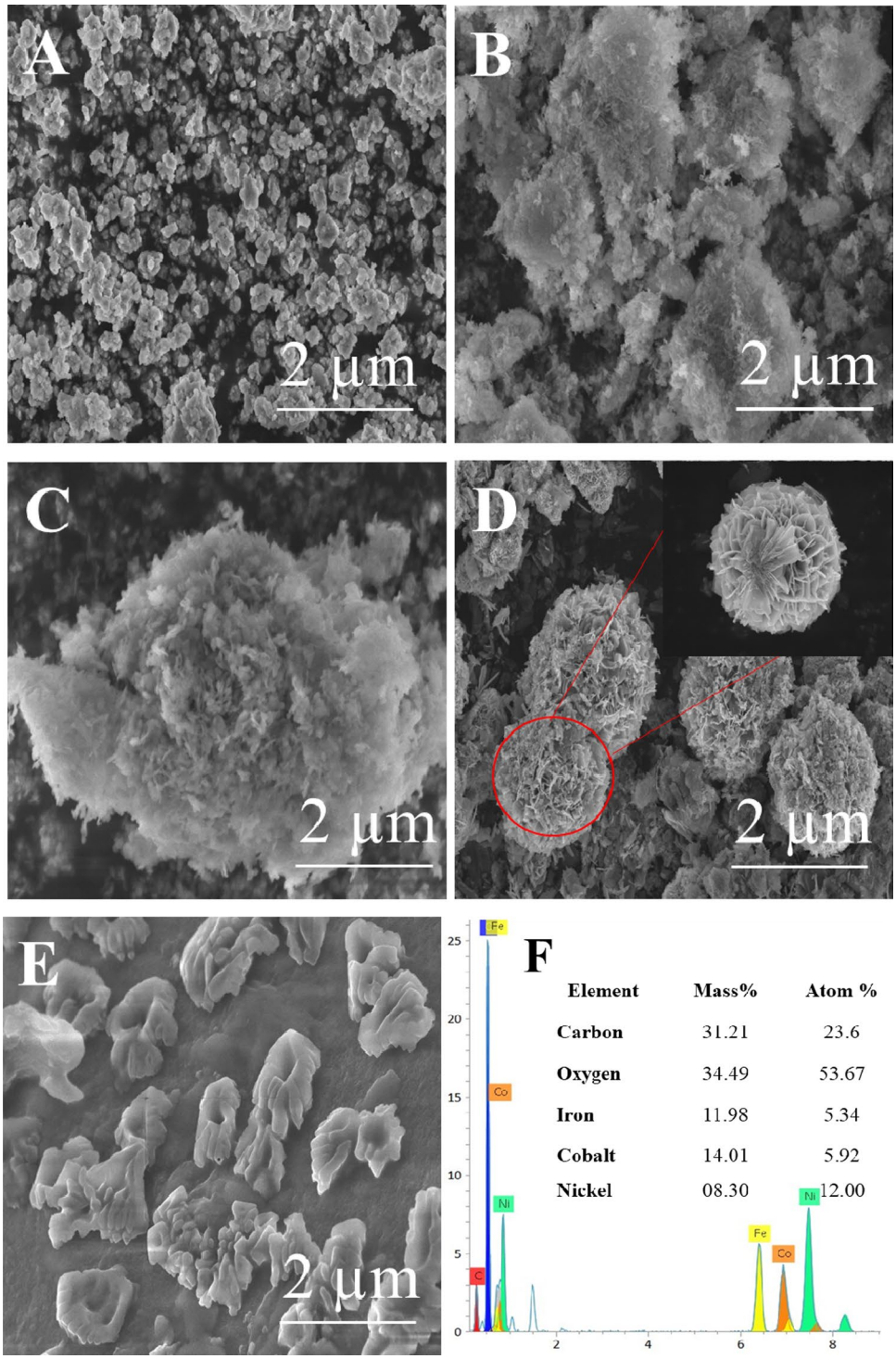

Fig. 3 FE-SEM images: **a** Co–Ni-LDH, **b** $Fe_{4\%}$/Co–Ni-LDH, **c** $Fe_{6\%}$/Co–Ni-LDH, **d** $Fe_{8\%}$/Co–Ni-LDH, **e** $Fe_{10\%}$/Co–Ni-LDH and **f** EDX spectrum of $Fe_{8\%}$/Co–Ni-LDH

platform channel for ion penetration and intimate contact, which is necessary for significant immobility [45].

In addition to the excellent ORR process, prepared LDHs were also used for OER in the same electrolyte (0.1 M KOH), $Fe_{8\%}$/CoNi-LDH shows lower overpotential (232 mV, Fig. 8a, Table 4), and maximum current density (14.23 mA cm^{-2}) among other samples (Fig. 8). This is comparable to the performance of recorded OER electrocatalysts (Table S1), and to summarized OER catalysts in Fig. 8 and Table 4. The strong coupling effect between the LDH and the coordinately unsaturated Ni, Co, and Fe sites that are exposed to it can explain this. Therefore, more accessible Fe sites resulting from the hierarchical open-channel structure of the LDHs increased the OER activity. Compared to the

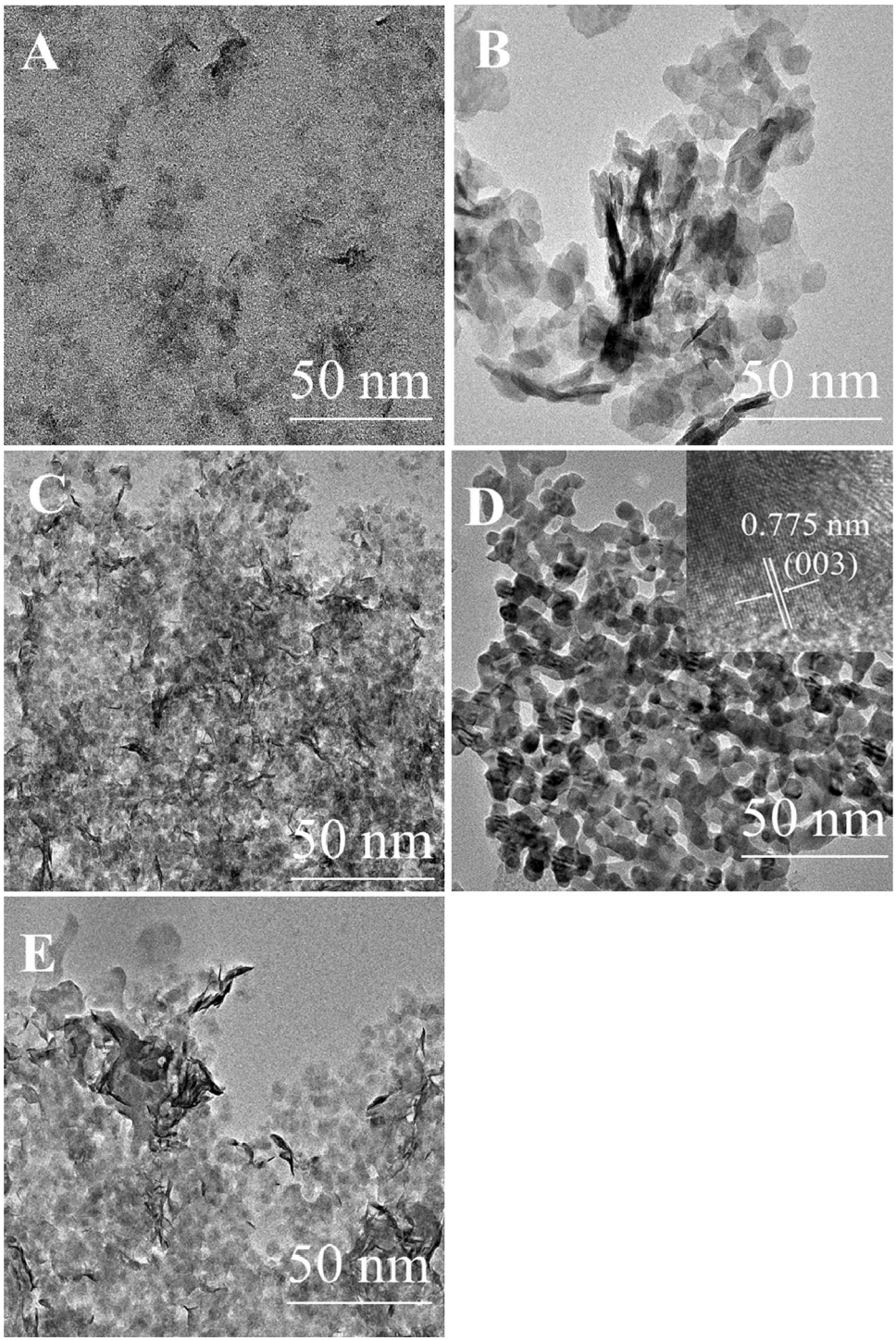

Fig. 4 TEM images: **a** CoNi LDH, **b** $Fe_{4\%}$/CoNi LDH, **c** $Fe_{6\%}$/CoNi LDH, **d** $Fe_{8\%}$/CoNi LDH (inserted HRTEM image) and **e** $Fe_{10\%}$/CoNi LDH

most active noble-metal-free catalysts, $Fe_{8\%}$/CoNi-LDH had the lowest starting potential as well as the fastest current performance. The overpotential fell as integration with Fe increased. Aside from the synergistic effects between the transition metal cations, high conductivity is another important factor attributing to the superior OER activity of $Fe_{8\%}$/CoNi-LDH. Taking these results into account, it can be concluded that $Fe_{8\%}$/CoNi-LDH not only increased functional site activity but also increased the activity of the exposed sites by Fe and reverse micelles. Thus, the Fe_x/CoNi-composite demonstrates the superior OER activity, which can be verified by the robust liberation of bubbles from the electrode surface during the reaction process.

The durability of $Fe_{8\%}$/CoNi-LDH was calculated using chronoamperometric measurements at 1600 rpm in an N_2-saturated 0.1 M KOH solution, as shown in Fig. 8f. Apart

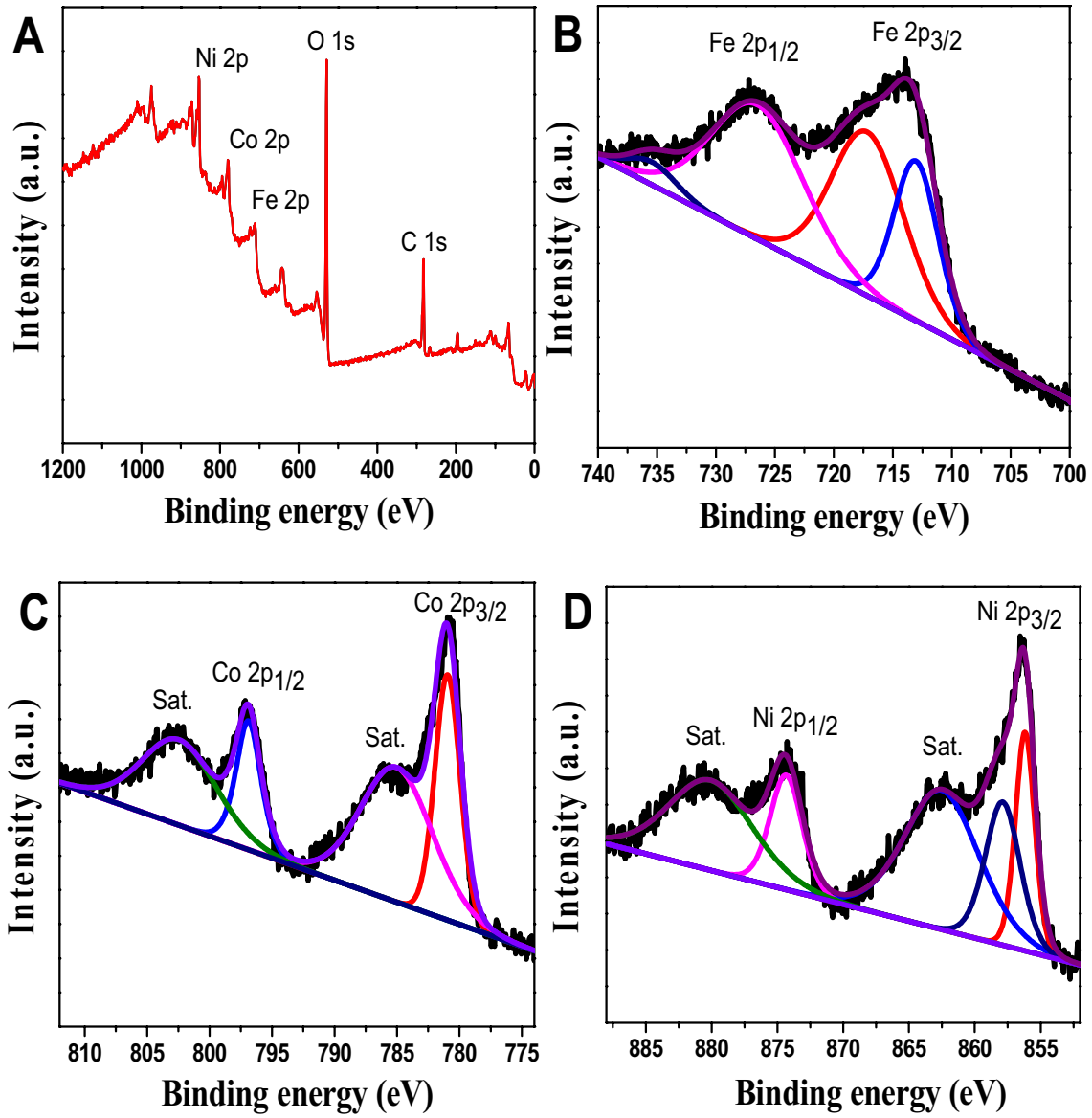

Fig. 5 XPS survey plot **a** of the $Fe_{8\%}$/Co–Ni-LDH and its corresponding HRXPS spectra of **b** Fe 2*p*, **c** Co 2*p*, and **d** Ni 2*p*

from superior performance, $Fe_{8\%}$/CoNi-LDH also demonstrated robust stability. It has preserved 92.1% of the existing capacity after continuous operation for the 80,000 s. By contrast, the current density of the commercial RuO_2 catalyst showed a sharp decrease to 79.4%. After 1000 continuous scanning, there is practically no decline in both its starting potential and current density, and only a few negative shifts meet its half-wave potential. The exceptional electrochemical stability of catalyst can be due to the homogeneous hybridization of Fe nanoparticles and building blocks of LDH. The new functional sites are similarly exposed to keep the catalytic efficiency constant after the degradation of the catalyst's surface. The hydroxy-bridging relation, meanwhile, connects metal cations in the layers [19–21]. Lewis-acid cations can modulate the properties of certain hydroxy groups in the ligand fields [38]. Second, there may be one real impact in Fe's electronic structure. The electronic structure of Fe is suitable for conductivity, the motion of ions, trapping of electrons, and chemisorption. These three factors contribute to the formation of a highly active catalyst for doped LDH CTAB-caped Fe nanoparticles [28–30]. Although similar positive effects on OER activity have recently been recorded in LDH, it is not well documented how structure and preparation approaches affect the electrochemical activity and interact with Ni or Fe in LDH materials as well as further study is desired, particularly in situ or ours results suggest.

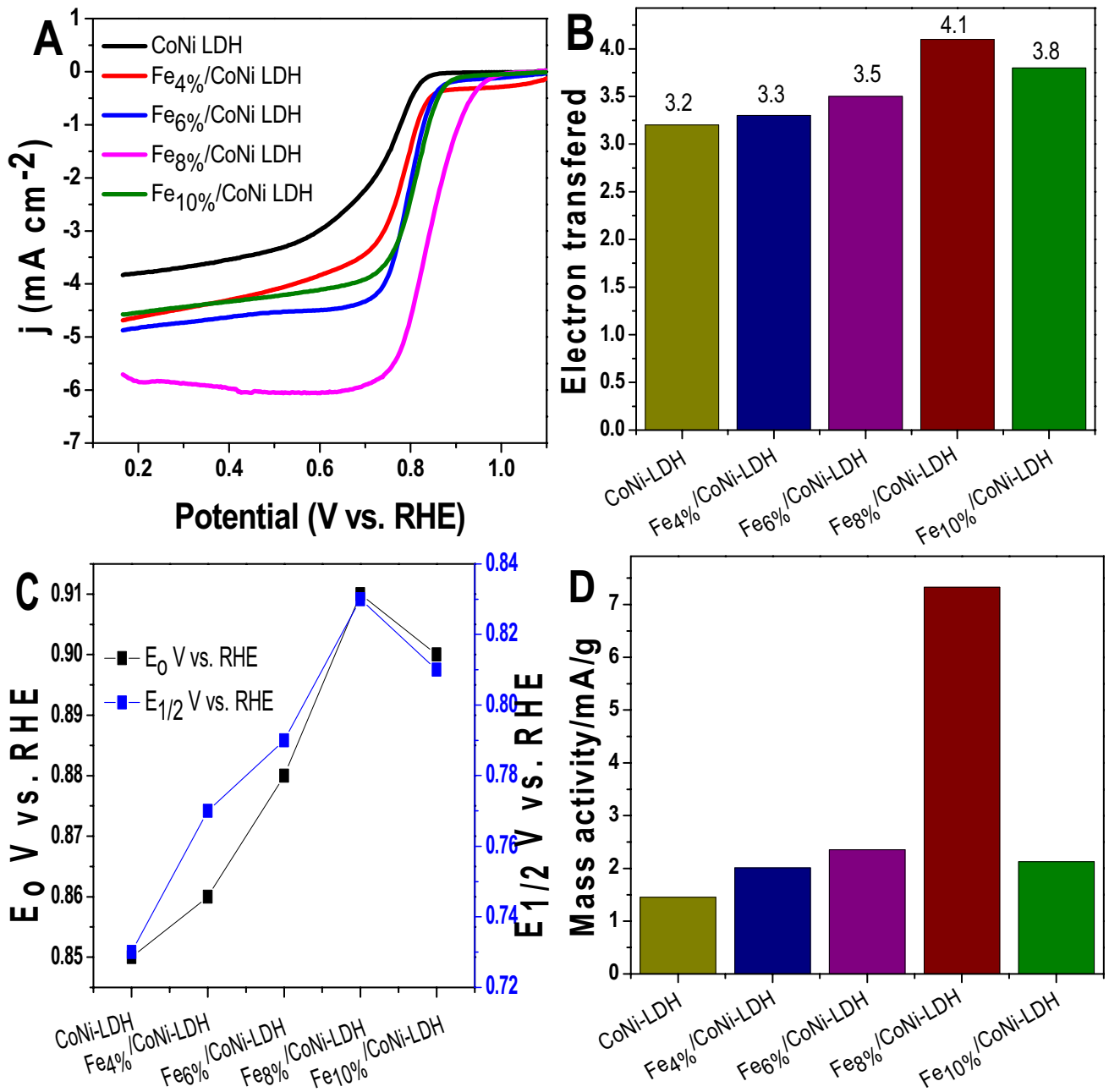

Fig. 6 ORR analysis: **a** LSV curves of various prepared LDHs recorded at 1600 rpm with a scan rate of 10 mV s^{-1} in 0.1 M KOH at room temperature, **b** number of electrons transferred, **c** comparison of E_o and $E_{1/2}$, and **d** mass activity of various LDHs

Table 3 ORR parameters of prepared catalysts

Catalysts	E_o (E vs. RHE)	$E_{1/2}$ (E vs. RHE)	MA (mA/mg)	n
Co–Ni-LDH	0.85	0.73	1.45	3.2
$Fe_{4\%}$/Co–Ni-LDH	0.86	0.77	2.01	3.3
$Fe_{6\%}$/Co–Ni-LDH	0.88	0.79	2.35	3.5
$Fe_{8\%}$/Co–Ni-LDH	0.91	0.83	7.33	4.1
$Fe_{10\%}$/Co–Ni-LDH	0.90	0.81	2.125	3.8

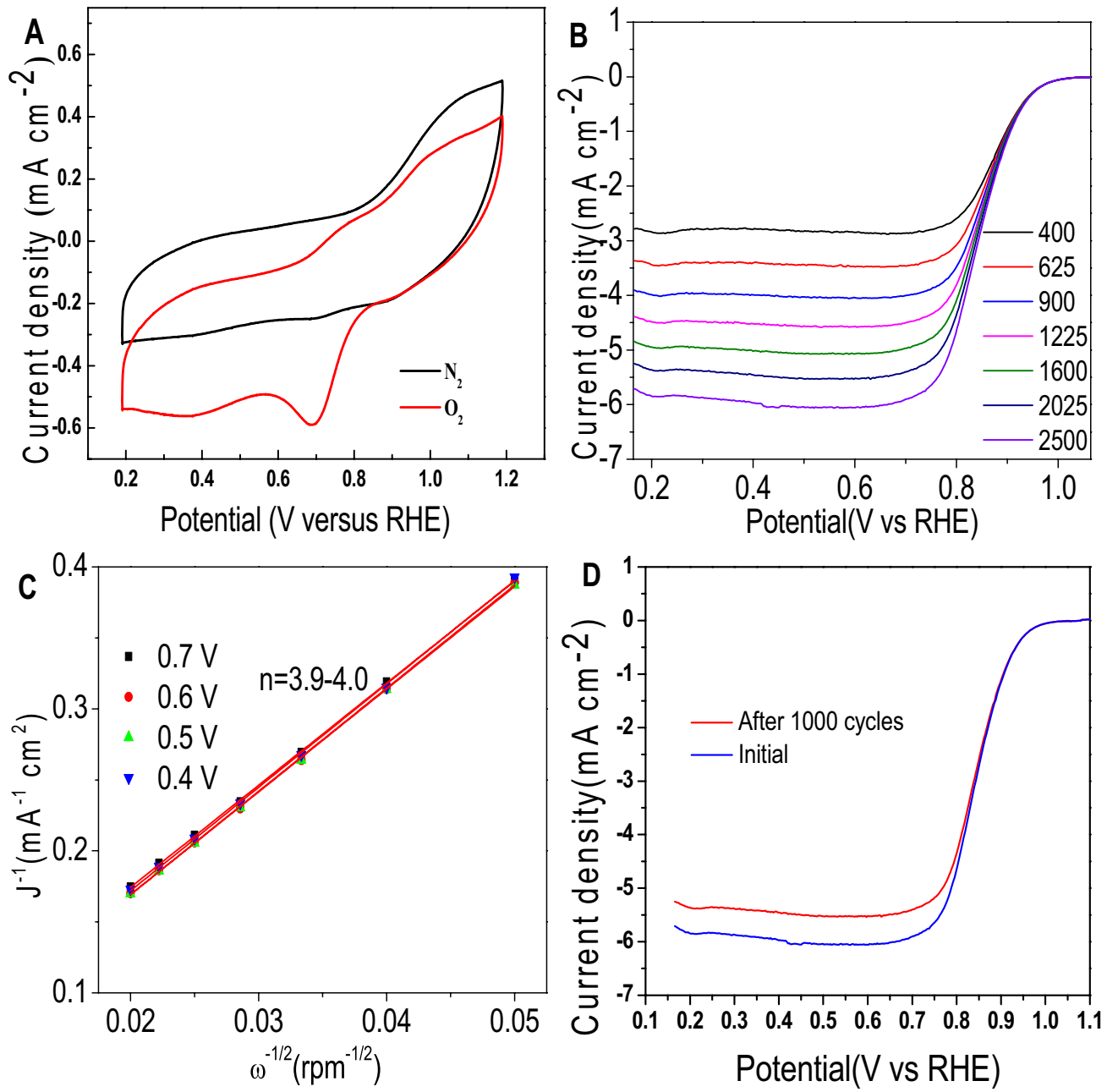

Fig. 7 ORR parameters of $Fe_{8\%}$/Co–Ni-LDH: **a** CV curves in O_2/N_2 environment, **b** LSV curves recorded at various rotating speeds in O_2-saturated 0.1 M KOH solution at 10 mV s^{-1}, **c** Koutecky–Levich plots recorded at different potentials, and **d** LSV curves recorded before and after 1000 cycles of CV

The excellent electrocatalytic activity of $Fe_{8\%}$/Co–Ni LDH is attributed to the following features: First, the modular 2D layered structure of LDH materials has favorable charge transfer due to the redox features of multivalent metal cations in the layers at certain potentials [5–13]. Intercalated anions migrate within the interlayer space to balance the dynamic change of the positive charges in the layers during electrochemical reactions [19–22]. Second, enhancing electronic interactions within the metal hydroxide matrix typically has a positive effect on activity, with possible synergistic roles between redox-active cations (Ni, Fe, and Cr) and Lewis-acid cations (Fe and Cr) [25–29]. Redox-active cations with high oxidation states (Ni^{3+}, Ni^{4+}; Fe^{3+}, Fe^{4+}) are likely to be the effective active sites in catalysts [31–33]. The addition of Fe cations with Fe^{3+}, and possibly Fe^{4+} oxidation states can buffer the multielectron process necessary for water oxidation [39–42].

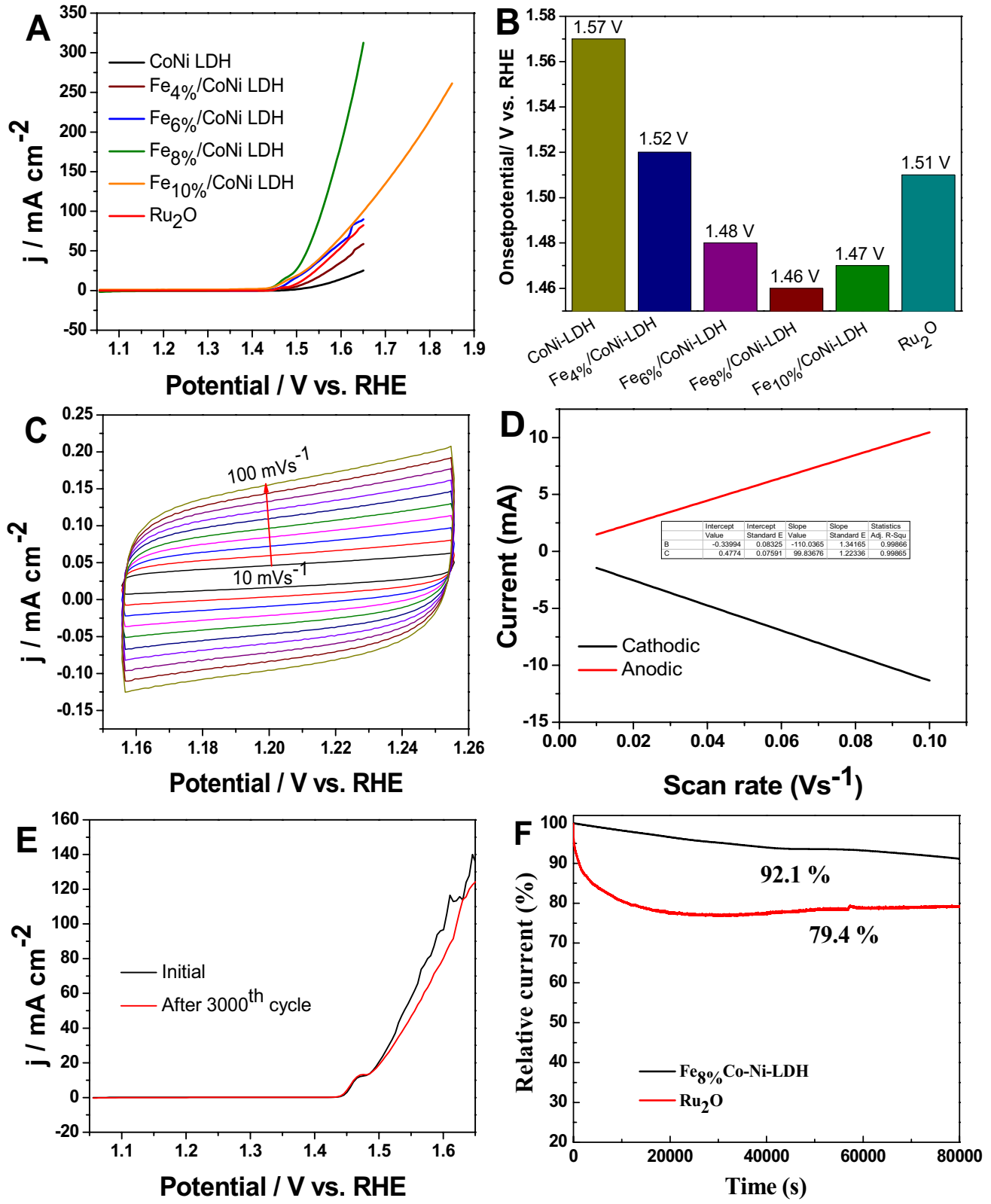

Fig. 8 OER analysis: **a** LSV curves of various prepared LDHs and commercial Ru_2O, at 1600 rpm in 0.1 M KOH solution, **b** comparison of overpotentials various catalysts, **c** CV curves of $Fe_{8\%}$/Co–Ni-LDH at different scan rates in N_2-saturated environment, **d** curve of current vs. scan rates of $Fe_{8\%}$/Co–Ni-LDH, **e** LSV curves of $Fe_{8\%}$/Co–Ni-LDH recorded initially. After 1000 CV cycles, and **f** *i–t* curve of $Fe_{8\%}$/Co–Ni-LDH and Ru_2O recorded at 1600 rpm in the N_2-saturated environment for 10 h

Table 4 OER parameters of prepared catalysts and commercial RuO_2

Catalysts	$\eta_{10\ mAcm-2}$ (mV)	Onset potential V (RHE) ($j = 10$ mA cm^{-2})	$J\ \eta = 0.25$ V (mA cm^{-2})	Tafel slope (mV/dec)	ΔE
Co–Ni-LDH	340	1.57	0.396	78	0.84
$Fe_{4\%}$/Co–Ni-LDH	294	1.52	2.97	70	0.75
$Fe_{6\%}$/Co–Ni-LDH	251	1.48	10.30	46	0.69
$Fe_{8\%}$/Co–Ni-LDH	232	1.46	14.23	25	0.63
$Fe_{10\%}$/Co–Ni-LDH	242	147	13.21	38	0.66
RuO_2	275	151	4.49	40	-

The $Fe_{8\%}$/Co–Ni LDH electrocatalyst has a large surface area, due to the small size of the nanoparticles, which shorten the transport distance and increase the kinetics of the reactions and high mesoporosity which boost the mass transport of the reactants and products during the ORR catalysis resulting in the accomplishment of efficient reaction kinetics [23–26]. The structure of $Fe_{8\%}$/Co–Ni LDH could trap and transfer O_2 molecule to catalytic sites due to the optimum composition, more uniform dispersed Fe nanoparticles and large specific surface area, while the uniformly dispersed Fe NPs provide adequate active sites to transform O_2 leading to superior activity [23–27]. Importantly, Fe atoms-doping not only could work synergistically with metal species to provide more active sites but also induce the uneven charge distribution, resulting in superior performance [9–13]. These results suggest this trimetallic design is effective and could provide a general strategy to improve the activity, performance, and stability of the promising bifunctional catalysts in the future.

Conclusion

The results show that the CTAB-capped Fe NPs are highly active and stable electrocatalyst for both ORR and OER. $Fe_{8\%}$/CoNi-LDH catalyst has excellent ORR (0.91 V) and OER (232 mV) electrocatalytic activity. The high catalytic activity of $Fe_{8\%}$/CoNi-LDH may be due to the synergism between Ni, Fe and Co metals, as well as the modification of the electronic structure facilitated in the stable and rigid crystal structure of LDH materials. Such findings will open a new path for nanostructures to be adequately developed and produced as multifunctional electrocatalysts.

Acknowledgements The author wishes to express his sincere thanks to the laboratory facilities provided for this work in the School of Chemistry and Chemical Engineering, Shaanxi Normal University, Xi'an, China.

References

1. J. Li, C. Shu, Z. Ran, M. Li, R. Zheng, J. Long, Heteroatom-induced electronic structure modulation of vertically oriented oxygen vacancy-rich NiFe layered double oxide nanoflakes to boost bifunctional catalytic activity in Li–O_2 battery. ACS Appl. Mater. Interfaces **11**(33), 29868–29878 (2019)
2. R. Farhat, J. Dhainy, and L. Halaoui, OER catalysis at activated and co-deposited NiFe-oxo/hydroxide thin films is due to post-deposition surface-Fe and is not sustainable without Fe in solution. ACS Catal. acscatal.9b02580, 2019.
3. S. Li, W. Xie, Y. Song, and M. Shao, "Layered Double Hydroxide@Polydopamine Core-Shell Nanosheet Arrays-Derived Bifunctional Electrocatalyst for Efficient, Flexible, All-Solid-State Zinc-Air Battery," ACS Sustain. Chem. Eng., 2019.
4. X. Guo et al., Tuning the bifunctional oxygen electrocatalytic properties of core-shell Co_3O_4@NiFe LDH catalysts for Zn-air batteries: effects of interfacial cation valences. ACS Appl. Mater. Interfaces **11**(24), 21506–21514 (2019)
5. Y. Qian, T. An, E. Sarnello, Z. Liu, T. Li, D. Zhao, Janus electrocatalysts containing MOF-derived carbon networks and NiFe-LDH nanoplates for rechargeable zinc-air batteries. ACS Appl. Energy Mater. **2**(3), 1784–1792 (2019)
6. R. Majee, Q.A. Islam, S. Bhattacharyya, Surface charge modulation of perovskite oxides at the crystalline junction with layered double hydroxide for a durable rechargeable zinc-air battery. ACS Appl. Mater. Interfaces **11**(39), 35853–35862 (2019)
7. S.A. Chala et al., Site activity and population engineering of NiRu-layered double hydroxide nanosheets decorated with silver nanoparticles for oxygen evolution and reduction reactions. ACS Catal. **9**(1), 117–129 (2019)
8. K. Chakrapani et al., The role of composition of uniform and highly dispersed cobalt vanadium iron spinel nanocrystals for oxygen electrocatalysis. ACS Catal. **8**(2), 1259–1267 (2018)
9. N. Todoroki, T. Wadayama, Heterolayered Ni–Fe hydroxide/oxide nanostructures generated on a stainless-steel substrate for efficient alkaline water splitting. ACS Appl. Mater. Interfaces **11**, 44161–44169 (2019)
10. T. Bhowmik, M.K. Kundu, S. Barman, CoFe layered double hydroxide supported on graphitic carbon nitrides: an efficient and durable bifunctional electrocatalyst for oxygen evolution and hydrogen evolution reactions. ACS Appl. Energy Mater. **1**(3), 1200–1209 (2018)
11. G. Rajeshkhanna, T.I. Singh, N.H. Kim, J.H. Lee, Remarkable bifunctional oxygen and hydrogen evolution electrocatalytic activities with trace-level Fe doping in Ni- and Co-layered double hydroxides for overall water-splitting. ACS Appl. Mater. Interfaces **10**(49), 42453–42468 (2018)
12. F. Davodi et al., Catalyst support effect on the activity and durability of magnetic nanoparticles: toward design of advanced electrocatalyst for full water splitting. ACS Appl. Mater. Interfaces **10**(37), 31300–31311 (2018)
13. J.M. Barforoush, T.E. Seuferling, D.T. Jantz, K.R. Song, K.C. Leonard, Insights into the active electrocatalytic areas of layered double hydroxide and amorphous nickel-iron oxide oxygen

evolution electrocatalysts. ACS Appl. Energy Mater. **1**(4), 1415–1423 (2018)
14. F. Wang et al., Advanced electrocatalytic performance of Ni-based materials for oxygen evolution reaction. ACS Sustain. Chem. Eng. **7**(1), 341–349 (2019)
15. Z. Zand et al., Nickel-vanadium layered double hydroxide under water-oxidation reaction: new findings and challenges. ACS Sustain. Chem. Eng. **7**(20), 17252–17262 (2019)
16. B.J. Waghmode, A.P. Gaikwad, C.V. Rode, S.D. Sathaye, K.R. Patil, D.D. Malkhede, Calixarene intercalated NiCo layered double hydroxide for enhanced oxygen evolution catalysis. ACS Sustain. Chem. Eng. **6**(8), 9649–9660 (2018)
17. K. Wang, W. Wu, Z. Tang, L. Li, S. Chen, N.M. Bedford, Hierarchically structured $Co(OH)_2$/CoPt/N-CN air cathodes for rechargeable zinc-air batteries. ACS Appl. Mater. Interfaces **11**(5), 4983–4994 (2019)
18. S. Dutta, A. Indra, Y. Feng, T. Song, U. Paik, Self-supported nickel iron layered double hydroxide-nickel selenide electrocatalyst for superior water splitting activity. ACS Appl. Mater. Interfaces **9**(39), 33766–33774 (2017)
19. S. Sirisomboonchai et al., Fabrication of NiO microflake@ NiFe-LDH nanosheet heterostructure electrocatalysts for oxygen evolution reaction. ACS Sustain. Chem. Eng. **7**(2), 2327–2334 (2019)
20. S. Sun, C. Lv, W. Hong, X. Zhou, F. Wu, G. Chen, Dual tuning of composition and nanostructure of hierarchical hollow nanopolyhedra assembled by layered double hydroxide nanosheets for efficient electrocatalytic oxygen evolution. ACS Appl. Energy Mater. **2**(1), 312–319 (2019)
21. A.C. Thenuwara et al., Cobalt intercalated layered NiFe double hydroxides for the oxygen evolution reaction. J. Phys. Chem. B **122**(2), 847–854 (2018)
22. M.S. Islam et al., Bifunctional 2D superlattice electrocatalysts of layered double hydroxide-transition metal dichalcogenide active for overall water splitting. ACS Energy Lett. **3**(4), 952–960 (2018)
23. M.A. Oliver-Tolentino et al., An approach to understanding the electrocatalytic activity enhancement by superexchange interaction toward OER in alkaline media of Ni-Fe LDH. J. Phys. Chem. C **118**(39), 22432–22438 (2014)
24. J.A. Carrasco, R. Sanchis-Gual, A. Seijas-Da Silva, G. Abellan, E. Coronado, Influence of the interlayer space on the water oxidation performance in a family of surfactant-intercalated NiFe-layered double hydroxides. Chem. Mater. **31**(17), 6798–6807 (2019)
25. K. Karthick, S. Anantharaj, S.R. Ede, S. Kundu, Nanosheets of nickel iron hydroxy carbonate hydrate with pronounced OER activity under alkaline and near-neutral conditions. Inorg. Chem. **58**(3), 1895–1904 (2019)
26. X. Feng et al., Facile synthesis of Co_9S_8 hollow spheres as a high-performance electrocatalyst for the oxygen evolution reaction. ACS Sustain. Chem. Eng. **6**(2), 1863–1871 (2018)
27. F. Amiripour, S. Ghasemi, and S.N. Azizi. Novel composite based on bimetallic AuNi-embedded nano X zeolite/MWCNT as a superior electrocatalyst for oxygen evolution reaction. ACS Sustain. Chem. Eng. (2019).
28. S. Samanta, S. Khilari, K. Bhunia, D. Pradhan, B. Satpati, R. Srivastava, Double-metal-ion-exchanged mesoporous zeolite as an efficient electrocatalyst for alkaline water oxidation: synergy between Ni–Cu and their contents in catalytic activity enhancement. J. Phys. Chem. C **122**(20), 10725–10736 (2018)
29. L. Trotochaud, S.L. Young, J.K. Ranney, S.W. Boettcher, Nickel-iron oxyhydroxide oxygen-evolution electrocatalysts: the role of intentional and incidental iron incorporation. J. Am. Chem. Soc. **136**(18), 6744–6753 (2014)
30. S. Parvin, D.K. Chaudhary, A. Ghosh, S. Bhattacharyya, Attuning the electronic properties of two-dimensional Co–Fe–O for accelerating water electrolysis and photolysis. ACS Appl. Mater. Interfaces **11**(34), 30682–30693 (2019)
31. F. Malara et al., A flexible electrode based on Al-doped nickel hydroxide wrapped around a carbon nanotube forest for efficient oxygen evolution. ACS Catal. **7**(7), 4786–4795 (2017)
32. A. Kumar, S. Bhattacharyya, Porous NiFe-oxide nanocubes as bifunctional electrocatalysts for efficient water-splitting. ACS Appl. Mater. Interfaces **9**(48), 41906–41915 (2017)
33. V. Vij et al., Nickel-based electrocatalysts for energy-related applications: oxygen reduction, oxygen evolution, and hydrogen evolution reactions. ACS Catal. **7**(10), 7196–7225 (2017)
34. A.K. Taylor, I. Andreu, M. Louie, and B.D. Gates. Electrochemically aged Ni Electrodes supporting $NiFe_2O_4$ nanoparticles for the oxygen evolution reaction. ACS Appl. Energy Mater. (2019).
35. S. Dutta, C. Ray, Y. Negishi, T. Pal, Facile synthesis of unique hexagonal nanoplates of Zn/Co hydroxy sulfate for efficient electrocatalytic oxygen evolution reaction. ACS Appl. Mater. Interfaces **9**(9), 8134–8141 (2017)
36. A.K. Taylor, I. Andreu, B.D. Gates, Regular dimpled nickel surfaces for improved efficiency of the oxygen evolution reaction. ACS Appl. Energy Mater. **1**(4), 1771–1782 (2018)
37. U.Y. Qazi et al., One-step growth of iron-nickel bimetallic nanoparticles on FeNi alloy foils: highly efficient advanced electrodes for the oxygen evolution reaction. ACS Appl. Mater. Interfaces **9**(34), 28627–28634 (2017)
38. L. Liardet, X. Hu, Amorphous cobalt vanadium oxide as a highly active electrocatalyst for oxygen evolution. ACS Catal. **8**(1), 644–650 (2018)
39. S. Anantharaj, P.N. Reddy, S. Kundu, Core-oxidized amorphous cobalt phosphide nanostructures: an advanced and highly efficient oxygen evolution catalyst. Inorg. Chem. **56**(3), 1742–1756 (2017)
40. A. Munir, T.U. Haq, A. Qurashi, H.U. Rehman, A. Ul-Hamid, I. Hussain, Ultrasmall Ni/NiO nanoclusters on thiol-functionalized and-exfoliated graphene oxide nanosheets for durable oxygen evolution reaction. ACS Appl. Energy Mater. **2**(1), 363–371 (2019)
41. C.G. Read, J.F. Callejas, C.F. Holder, R.E. Schaak, General strategy for the synthesis of transition metal phosphide films for electrocatalytic hydrogen and oxygen evolution. ACS Appl. Mater. Interfaces **8**(20), 12798–12803 (2016)
42. J. Ryu, N. Jung, J.H. Jang, H.J. Kim, S.J. Yoo, In situ transformation of hydrogen-evolving CoP nanoparticles: toward efficient oxygen evolution catalysts bearing dispersed morphologies with co-oxo/hydroxo molecular units. ACS Catal. **5**(7), 4066–4074 (2015)
43. B. Sarkar, B.K. Barman, K.K. Nanda, Non-precious bimetallic CoCr nanostructures entrapped in bamboo-like nitrogen-doped graphene tube as a robust bifunctional electrocatalyst for total water splitting. ACS Appl. Energy Mater. **1**(3), 1116–1126 (2018)
44. S. Anantharaj, S.R. Ede, K. Sakthikumar, K. Karthick, S. Mishra, S. Kundu, Recent trends and perspectives in electrochemical water splitting with an emphasis on sulfide, selenide, and phosphide catalysts of Fe Co, and Ni: a review. ACS Catal. **6**(12), 8069–8097 (2016)
45. S. Anantharaj et al., Shrinking the hydrogen overpotential of Cu by 1V and imparting ultralow charge transfer resistance for enhanced H_2 evolution. ACS Catal. **8**(7), 5686–5697 (2018)
46. N. Weidler et al., X-ray photoelectron spectroscopic investigation of plasma-enhanced chemical vapor deposited NiOx, NiOx (OH) y, and CoNiOx (OH)y: influence of the chemical composition on the catalytic activity for the oxygen evolution reaction. J. Phys. Chem. C **121**(12), 6455–6463 (2017)
47. K. Karthick et al., Advanced Cu_3Sn and selenized Cu_3Sn@Cu foam as electrocatalysts for water oxidation under alkaline and near-neutral conditions. Inorg. Chem. **58**(14), 9490–9499 (2019)

48. M. Gorlin et al., Tracking catalyst redox states and reaction dynamics in Ni–Fe oxyhydroxide oxygen evolution reaction electrocatalysts: The role of catalyst support and electrolyte pH. J. Am. Chem. Soc. **139**(5), 2070–2082 (2017)
49. S. Anantharaj, K. Karthick, S. Kundu, Spinel cobalt titanium binary oxide as an all-non-precious water oxidation electrocatalyst in acid. Inorg. Chem. **58**(13), 8570–8576 (2019)
50. D.T. Jantz, K.C. Leonard, Characterizing electrocatalysts with scanning electrochemical microscopy. Ind. Eng. Chem. Res. **57**(22), 7431–7440 (2018)
51. R.V. Digraskar, V.S. Sapner, A.V. Ghule, B.R. Sathe, Enhanced overall water-splitting performance: oleylamine-functionalized GO/Cu_2ZnSnS_4 composite as a Nobel metal-free and nonprecious electrocatalyst. ACS Omega **4**, 18969–18977 (2019)
52. S. Anantharaj, K. Karthick, P. Murugan, and S. Kundu. V^{3+} incorporated β-$Co(OH)_2$: a robust and efficient electrocatalyst for water oxidation. Inorg. Chem. (2019).

Affiliations

Anand Parkash[1,2]

[1] Key Laboratory of Applied Surface and Colloid Chemistry (Shaanxi Normal University), Ministry of Education, Xi'an 710119, People's Republic of China

[2] School of Chemistry and Chemical Engineering, Shaanxi Normal University, Chang'an West Street 620, Xi'an 710119, People's Republic of China